Compressed Sensing on Multi-pinhole Collimator SPECT Camera for Sentinel Lymph Node Biopsy

Carlo Seppi[1(✉)], Uri Nahum[1], Peter A. von Niederhäusern[1], Simon Pezold[1], Michael Rissi[2], Stephan K. Haerle[3], and Philippe C. Cattin[1]

[1] Center for medical Image Analysis and Navigation (CIAN),
Department of Biomedical Engineering, University of Basel, Allschwil, Switzerland
`carlo.seppi@unibas.ch`
[2] Head of Research and Physics, DECTRIS Ltd., Baden-Daetwil, Switzerland
[3] Head and Neck Surgical Oncology, Hirslanden Clinic St. Anna Lucerne,
Luzern, Switzerland

Abstract. State-of-the-art imaging devices for sentinel lymph node biopsy are either a 1-dimensional gamma probe or more recently 2-dimensional gamma cameras that locate the sentinel lymph node. These devices, however, share difficulties when multiple lymph nodes are close-by and do not allow the estimation of the distance to the lymph nodes, as the tracer activation is projected either to a 1- or 2-dimensional image plane. We propose a method, which reconstructs the tracer distribution using a single image of the detector resulting from a multi-pinhole colli-mator. Applying standard image processing tools on the detector's image leads to a reduced, sparse system. Thus, we propose an efficient and reliable compressed sensing strategy, to reconstructs the 3-dimensional tracer distribution using a multi-pinhole collimator and a single detector image. This approach enables better estimation of lymph nodes position and improves the differentiation of close-by lymph nodes.

1   Introduction

Oral and oropharyngeal squamous cell carcinoma is a common type of cancer in the head and neck area. If initial staging indicates a wide spread of cancer, standard of care involves complete surgical removal of the lymphatics, a so-called neck dissection. It is of utmost importance to stage the neck as concise as possi-ble, since lymphatic involvement of the neck is the single most important survival parameter. Traditionally a neck dissection has been the standard procedure for neck staging. Recent studies have shown, that this radical procedure is required in less than 30% of the patients with the clinical lack of lymphatic involvement. Hence, in sentinel lymph node biopsy (SNB) the first lymph node in the drainage basin is analyzed for cancerous cells and neck dissection is only performed when positive cells are present. Besides staging the cancer, it is crucial to know if the tumor has spread to the lymphatics and to exclude such regional spread. One possible staging and treatment method for head and neck squamous cell carcinoma (HNSCC) is neck dissection. The neck contains dozens of lymphatic

vessels and draining nodes in a complex anatomic area. The procedure harbors a variety of potential risks, such as nerve injury (resulting in shoulder dysfunction, dysphagia, or facial asymmetry) or lymphatic edema.

Similar to head and neck cancer, in melanoma or breast cancer, lymphatic spread has a major impact on the patient's outcome. For the latter two cancer types, SNB is considered to be the standard staging procedure. Recent studies have shown that for selected head and neck tumors, SNB seems to be an efficient staging procedure as well. Furthermore, in a clinically negative neck SNB, seems to be the most accurate histologic staging procedure with a high success rate in detecting occult disease.

The hypothesis is that the sentinel lymph node (SLN) is the first draining lymph node for a tumor of a specific site, while all the other lymph nodes will only be reached subsequently. A tumor can thus only have spread if cancerous cells can be detected in the SLN. Accordingly, complete neck dissection is only indicated if the SLN contains tumor cells.

Single-photon emission tomography (SPECT) combined with computed tomography (CT) is nowadays considered the standard method for preoperative imaging prior to any SNB. Thanks to the higher spatial resolution a better anatomical orientation is achieved compared to the classical lymphoscintigraphy (LS) alone. The company SurgicEye[1] sells a commercially available system based on freehand SPECT. However, a number of preparative steps are needed: first, reference targets have to be fixed onto the gamma probe and the patient, then the gamma activity will be registered in order to build a correct synthetic 3D model of the tumor and its location. The model is then used to produce an augmentation of the surgical scene and displayed on an external screen [8]. SPECT with multi-pinhole collimator [9] has been used to gain a better resolution of the SPECT-image. However, this can not be used for a fast diagnosis in the operation room. To summarize the aforementioned devices are not handy and do not reconstruct the depth of radioactive sources from a single image from the detector.

Compressed sensing is being used in many different areas, for example in MRI [5], one pixel camera [3], and recently Besson et al. [2] used compressed sensing in ultrasound. Compressed sensing has been proven to be a good approach to solve undetermined linear systems, where the solution is known to be sparse.

In this paper we introduce a method that combines images from a multi-pinhole collimator with compressed sensing to reconstruct the position of radioactive sources from a single image, which in a next step, may help to design a more handy device for radioactive source detection.

2   Materials and Methods

For our experiment we used a PILATUS3 gamma detector from DECTRIS Ltd. (5405 Baden-Daetwil, Switzerland) with a native resolution of 487×195 pixels,

---

each with a pixel size of $172\,\mu\text{m} \times 172\,\mu\text{m}$. The technology is based on direct detection of the gamma rays in the cadmium telluride sensor-material, which is hybridized with the PILATUS3 CMOS readout ASICs. In each pixel, the signals generated in the sensor are amplified, discriminated and counted. This technology allows to measure the incoming gamma ray flux without any readout noise.

Tungsten is an often used material in nuclear medicine to build a collimator. It has very good mechanical properties and a high specific density of $19.25\,\text{g/cm}^3$ and is thus also used for our collimator. The collimator design is based on [7]. It is placed on top of the detector, has the dimensions $86.9\,\text{mm} \times 36\,\text{mm} \times 36\,\text{mm}$. It has 8×3 compartments and in the center of each compartment there is a pinhole with a diameter of $1\,\text{mm}$ (see Fig. 1). The front and side plates have a thickness of $1\,\text{mm}$ and the septa have a thickness of $0.35\,\text{mm}$.
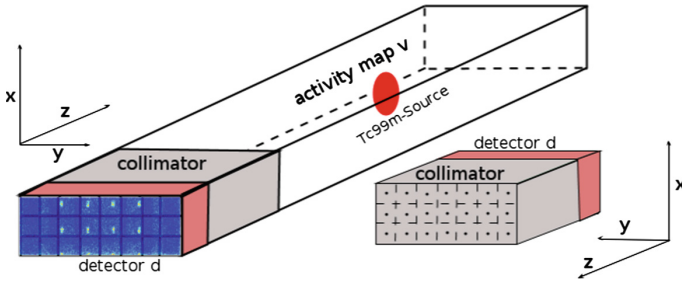

Fig. 1. The construction of an experiment: a map v of possible activities, detector d and a multi-pinhole collimator between them.

Our aim is to measure the radiation sources with a single image from the detector in relation to the position of the collimator using image processing and compressed sensing principles. The photons from the radiation sources of Technetium-99m (Tc-99m) are passing through the pinholes of the collimator and absorbed by the detector with a quantum efficiency of 50%.

Given radiation sources and a collimator, a map v of radiation activities in front of the collimator is defined. The relationship between the measured signal image on the detector d and the unknown activity map v (see Fig. 1) is given by

$$Av = d. \tag{1}$$

The visibility operator A is uniquely determined by the design of the collimator and translates through its multi-pinhole geometry, which activities can be seen by the detector d through the collimator's pinholes. To solve the system (1) A, v and d need to be discretized. First we discretize $\mathbf{d} \in \mathbb{R}_{\geqslant 0}^N$ and $\mathbf{v} \in \mathbb{R}_{\geqslant 0}^M$, where N and M are the degrees of freedom in the spatial discretization of the detector and area of interest in front of the collimator respectively. Next, we discretize the

visibility matrix $\mathbf{A} \in \{0,1\}^{N \times M}$: the entry $\mathbf{A}_{ij}$ is set to 1 if a possible activity $\mathbf{v}_j$ can be seen by the i-th entry of the detector $\mathbf{d}$.

Image Preprocessing: The original image given by the detector contains some irrelevant information, which mainly results from the photons penetrating through the walls of the collimator. To extract only useful information, we want to separate it from these artefacts.

Clearly the detector $\mathbf{d}$ should have zero entries at the positions where the collimator's walls meet the detector, hence we set those artificially to zero in $\mathbf{d}$ (see Fig. 2, first row). Removing further irrelevant information and smoothing the image is achieved by applying *Total Variation denoising*, namely

$$\min_{\mathbf{X}}\{||\mathbf{X} - \mathbf{d}||^2 + 2\lambda||\mathbf{X}||_{TV} : 0 \leq \mathbf{X}_{ij} \leq u\}, \tag{2}$$

where $\mathbf{d} \in \mathbb{R}^{m \times n}$ is the image of the detector, $\lambda \in [1,2]$ is a weighting factor, u is the upper bound of all pixels and $||\cdot||_{TV}$ is the discrete TV semi-norm as defined in [1]. The result of this method is displayed on the second row of Fig. 2. Next, we sparsify the resulting image, in a way that it contains non-zero entries only in the location of the critical data and thus holds a small number of non-zero entries: we apply sparsity as in [4] and set

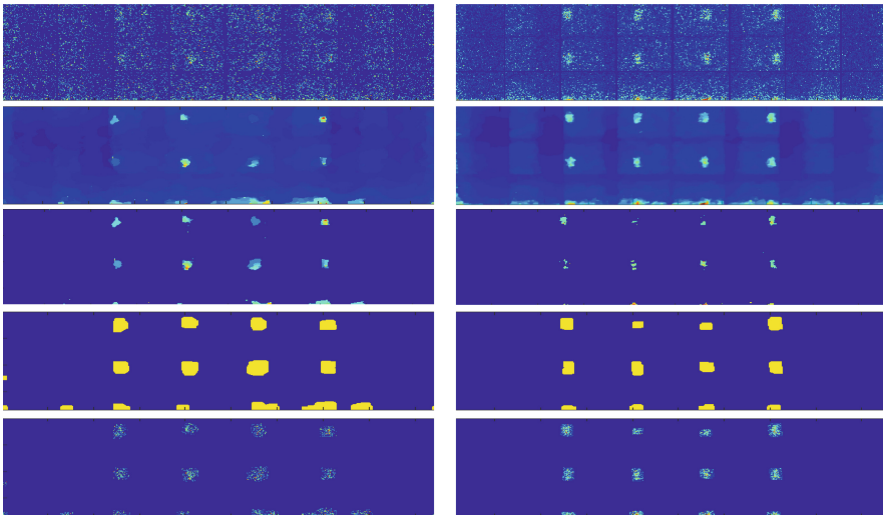$$d_j = \begin{cases} d_j, & d_j \geq \alpha||\mathbf{d}||_\infty \\ 0, & \text{else} \end{cases} \tag{3}$$

Fig. 2. Image processing of the detector $\mathbf{d}$ for two different exposure times $t = 5\,\mathrm{s}$ (left) and $t = 30\,\mathrm{s}$ (right). From top to bottom: detector image with collimator's walls position set to 0; Total Variation denoising; sparsified image; Gauss-filtered mask; end-result $\hat{\mathbf{d}}$.

for $j = 1, \ldots, N$ and $\alpha \in [0, 1)$. In the third row of Fig. 2 we show the sparsified version of the detector $\mathbf{d}$ image using (3). In addition, we apply the median filter to eliminate isolated pixels of the resulting sparsified detector image $\mathbf{d}$. To expand those areas and avoid over-filtering we use a standard Gaussian filter ($\sigma = 2$ pixels). The result of this expansion is shown in the fourth row of Fig. 2. The non-zero entries describe the position of the most concentrated radioactivity absorbed by the detector. Hence, we use those non-zero entries of the Gauss-filtered result as a mask on the original image (see Fig. 2, bottom). We define the resulting image as the filtered detector vector image $\hat{\mathbf{d}}$ and we use it in the following to reconstruct the position of the radiation sources.

Compressed Sensing: Recall that our aim is to find the positions of radioactivity in front of the collimator. Those are given by non-zero entries in the activity vector $\mathbf{v}$. To reduce the computational complexity, we take advantage of the geometric structure of the collimator and the sparsified detector image $\hat{\mathbf{d}}$ described above, to predict in which areas of $\mathbf{v}$ no activity is possible. This enables limiting the search space for $\mathbf{v}$ and we now may set a large number of its entries to zero. This results in a reduced vector $\hat{\mathbf{v}} \in \mathbb{R}^{\hat{M}}$, with $\hat{M} \ll M$.

The reduction in the dimension of $\hat{\mathbf{v}}$ allows us to reduce dramatically the size of the visibility matrix $\mathbf{A}$: for all $\mathbf{v}_i = 0$ we eliminate the i-th column of the matrix $\mathbf{A}$. This results in a reduced linear system

$$\hat{\mathbf{A}}\hat{\mathbf{v}} = \hat{\mathbf{d}}. \tag{4}$$

Since our solution $\hat{\mathbf{v}}$ is sparse we can now use the standard compressed sensing algorithm *weighted projected gradient for l_1 minimization* (WSPGL1), to solve the linear system (4) with

$$\min_{\hat{\mathbf{v}}} ||\hat{\mathbf{v}}||_{1,w} , \quad \text{s.t.} \quad ||\hat{\mathbf{A}}\hat{\mathbf{v}} - \hat{\mathbf{d}}||_2 \leq \varepsilon, \tag{5}$$

where $w \in (0, 1]^{\hat{M}}$ and $||\hat{\mathbf{v}}||_{1,w} := \sum_i w_i |\hat{v}_i|$ is the weighted l_1 norm; for details see [6].

In order to get quantitative rather just qualitative activity information in $\hat{\mathbf{v}}$ we have to take into account the fact that the photon density decreases with quadratic dependency over the distance. Hence, we need to weight the entries of $\hat{\mathbf{v}}$ as follows:

$$\mathbf{v}_i^w = \hat{\mathbf{v}}_i \left(\frac{h_i}{\min_j h_j} \right)^2 , \quad \text{for } i = 1, \ldots, M, \tag{6}$$

where $h_i > 0$ denotes the distance between the detector and the entry $\hat{\mathbf{v}}_i$. Now, $\mathbf{v}^w$ holds the information over the position of radioactivity in a 3D subspace in front of the collimator.

For visualization purposes and to extract the coordinates of the radiation sources we sum $\mathbf{v}^w$ along each axis direction (for the definition of the axes, see Fig. 1). This results in three 2D projections on the $xy-$, $xz-$ and $yz-$plane.

To get smooth results, we apply Gaussian filters on those sums ($\sigma = 2$ pixels on $xy-$ and $\sigma = 3$ pixels on $xz-$, $yz-$planes). Those three sums will be our main tool for finding the coordinates of the radiation sources, as shown in the following experiments.

3   Results

In contrast to the commonly used gamma cameras for SNB the proposed system provides the three-dimensional tracer distribution in the target area using a single image. To quantitatively validate its performance we devised a measurement series with a single or multiple tracer sources in the measurement area. For this will filled Eppendorfer tubes with a hight of 12 mm and a diameter of 7 mm with Tc-99m and an initial maximum activity of 20 MBq/0.5 mL.

In our experiments we used four different combinations of the tubes (see top of Fig. 3). The different Eppendorfer tubes simulated various lymph nodes. The tubes had different activity levels: ① represents a strong source, ② represents a slightly weaker one and ③ simulates a weak source. In each of the four experiments displayed in Fig. 3, we used an exposure time of 30 s from the radioactive source and placed the collimator 115 mm from it.
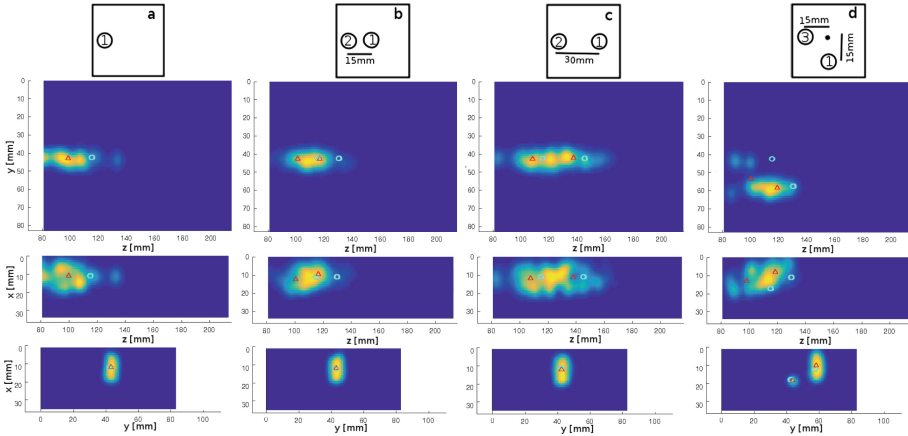

Fig. 3. From left to right: the four different experiments, with different source positions and strength illustrated on top of the figure). Second to fourth row, from top to bottom: projection of $\mathbf{v}^w$ in $yz-$, $xz-$ and $xy-$direction. Here, ○ denotes the true position of the source; △ is the computed position of our approach.

During the evaluation of the data, we noticed, that a minimum distance of 80 mm between the radioactive sources and the collimator is needed. This seems obvious as the radioactive source should be seen through multiple pinholes for optimal reconstruction. This is, however, clinically not a problem or even a

desired property as the sensor does not need to be placed too close to the patient. Hence, we set the entries of the activity map $\mathbf{v}_i$ to be zero, if the distance between $\mathbf{v}_i$ and the collimator was smaller than 80 mm.

In Fig. 3 we see the true position of the radioactive sources marked with $\bigcirc$) together with the results of our experiment (marked with $\triangle$, see below). The positions are shown on the $yz-$, $xz-$ and $xy-$plane (from second row to bottom). The results show a very high accuracy in the $xy-$direction, i.e. in the frontal perspective (Fig. 4, bottom) and a good approximation in terms of $yz-$, $xz-$axes. The results are summarized in Table 1.

Table 1. True and approximated radiation source coordinates with its L^2-error all values are given in millimeter [mm]

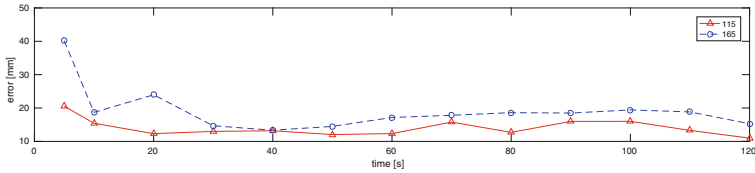|	True location		Approximation location		L^2-error
	First	Second	First	Second	
a	$(11, 41.5, 115)$	-	$(10.9, 42.9, 99.1)$	-	15.96
b	$(11, 41.5, 115)$	$(11, 41.5, 130)$	$(11.6, 42.8, 100.8)$	$(10.2, 42.9, 116.5)$	13.93
c	$(11, 41.5, 115)$	$(11, 41.5, 145)$	$(11.6, 42.6, 107.8)$	$(11.3, 42.4, 137.4)$	7.48
d	$(17, 41.5, 115)$	$(11, 56.5, 130)$	$(15.1, 48.5, 99.3)$	$(8.6, 58.3, 118.5)$	14.59

Fig. 4. Mean error over all different cases and projections, distances 115 mm and 165 mm.

We assume that the quality difference between the approximations in the $xy-$plane and the other two planes, are due to the collimator structure, which has only 3 pinholes in $x-$direction (see Fig. 1). Note that using a parallel-hole collimator, one may get only the frontal prospective and no depth information (similar to Fig. 3, bottom).

In order to determine the lower bound on the measurement time we repeated the above mentioned experiments, with different exposure times of $5, 10, 20, 30, 60$ and 120 s with the distances 115 mm and 165 mm of the collimator to source. The exposure time for $40, 50, 70, 80, 90, 100$ and 110 s were gained by summing respective measurement from the aforementioned series. To compute the error, we automatized the allocation of the radioactive sources using our results and compared them to the true values. This was done using Eq. (3) with $\alpha = 0.2$, k-means clustering and a Gaussian-fitting in each cluster. The x

value of the radioactive source is computed from the mean value of the approximations of the x location from the projection onto the $xy-$ and $xz-$plane, and analogously for the point's y and z location. Finally, the graph displayed in Fig. 4 is the mean value of all L^2-errors over the distances $115\,\text{mm}$ and $165\,\text{mm}$ in each projection and exposure time. The average L^2-error stays under $20\,\text{mm}$ for all the experiments involving more than $30\,\text{s}$ exposure, but does not show a considerable improvement afterwards.

4   Conclusion

In this paper, we presented a compressed sensing approach to reconstruct from a single image the positions of multiple radioactive tracer sources. Possible applications include but are not limited to sentinel lymph node biopsy with a clinically acceptable measurement time of only $30\,\text{s}$. We combined a multi-pinhole collimator with image filtering and a compressed sensing algorithm to reconstruct three-dimensional tracer distributions. The experiments showed a high accuracy of the tracer distribution in the frontal perspective and a good approximation in the depth of the radiation source. We believe, that simple improvements in the collimator structure i.e. adding more pinholes in the $x-$direction, or in other words a squared collimator/sensor configuration, would reduce the error further. The proposed approach enables a good estimation of lymph node positions and the differentiation in the depth of the lymph nodes with considerably smaller effort as compared to the established techniques. In the future we plan on integrating the detector system into an intra-operative navigation system.

References

1. Beck, A., Teboulle, M.: Fast gradient-based algorithms for constrained total variation image denoising and deblurring problems. IEEE Trans. Image Process. **18**(11), 2419–2434 (2009)
2. Besson, A., Carrillo, R.E., Bernard, O., Wiaux, Y., Thiran, J.P.: Compressed delay-and-sum beamforming for ultrafast ultrasound imaging. In: 2016 IEEE International Conference on Image Processing (ICIP), pp. 2509–2513, September 2016
3. Duarte, M.F., Davenport, M.A., Takbar, D., Laska, J.N., Sun, T., Kelly, K.F., Baraniuk, R.G.: Single-pixel imaging via compressive sampling. IEEE Sig. Process. Mag. **25**(2), 83–91 (2008)
4. Grote, M.J., Kray, M., Nahum, U.: Adaptive eigenspace method for inverse scattering problems in the frequency domain. Inverse Prob. **33**(2), 025006 (2017)
5. Lustig, M., Donoho, D., Pauly, J.M.: Sparse MRI: the application of compressed sensing for rapid MR imaging. Magn. Reson. Med. **58**(6), 1182–1195 (2007)
6. Mansour, H.: Beyond l_1-norm minimization for sparse signal recovery. In: 2012 IEEE Statistical Signal Processing Workshop (SSP), pp. 337–340, August 2012
7. von Niederhäusern, P.A., Maas, O.C., Rissi, M., Schneebeli, M., Haerle, S., Cattin, P.C.: Augmenting scintigraphy images with pinhole aligned endoscopic cameras: a feasibility study. In: Zheng, G., Liao, H., Jannin, P., Cattin, P., Lee, S.-L. (eds.) MIAR 2016. LNCS, vol. 9805, pp. 175–185. Springer, Cham (2016). doi:10.1007/978-3-319-43775-0_16

8. Okur, A., Ahmadi, S.A., Bigdelou, A., Wendler, T., Navab, N.: MR in OR: First analysis of AR/VR visualization in 100 intra-operative Freehand SPECT acquisitions. In: 2011 10th IEEE International Symposium on Mixed and Augmented Reality, pp. 211–218, October 2011

9. Rahman, T., Tahtali, M., Pickering, M.R.: An evaluation to design high performance pinhole array detector module for four head SPECT: a simulation study, vol. 9212, pp. 92120K–92120K-9 (2014). http://dx.doi.org/10.1117/12.2061634